nanomaterials

MDPI

Article

Incorporation of NiO into SiO_2, TiO_2, Al_2O_3, and $Na_{4.2}Ca_{2.8}(Si_6O_{18})$ Matrices: Medium Effect on the Optical Properties and Catalytic Degradation of Methylene Blue

Carlos Diaz [1,*], María L. Valenzuela [2], Olga Cifuentes-Vaca [3], Marjorie Segovia [1] and Miguel A. Laguna-Bercero [4,*]

1 Departamento de Química, Facultad de Química, Universidad de Chile, La Palmeras 3425, Nuñoa, Casilla 653, 7800003 Santiago de Chile, Chile; msmonrroy@gmail.com
2 Inorganic Chemistry and Molecular Material Center, Facultad de Ingeniería, Instituto de Ciencias Químicas Aplicadas, Universidad Autónoma de Chile, Av. El Llano Subercaseaux 2801, San Miguel, 8910060 Santiago de Chile, Chile; maria.valenzuela@uautonoma.cl
3 Departamento Ciencias Químicas, Facultad de Ciencias Exactas, Universidad Andres Bello, Sede Concepción, Autopista Concepción-Talcahuano, 7100 Talcahuano, Chile; olcifuen@hotmail.com
4 Instituto de Nanociencia y Materiales de Aragón (INMA), CSIC-Universidad de Zaragoza, 50009 Zaragoza, Spain
* Correspondence: cdiaz@uchile.cl (C.D.); malaguna@unizar.es (M.A.L.-B.)

Received: 13 November 2020; Accepted: 3 December 2020; Published: 10 December 2020

Abstract: The medium effect of the optical and catalytic degradation of methylene blue was studied in the NiO/SiO_2, NiO/TiO_2, NiO/Al_2O_3, and NiO/$Na_{4.2}Ca_{2.8}(Si_6O_{18})$ composites, which were prepared by a solid-state method. The new composites were characterized by XRD (X-ray diffraction of powder), SEM/EDS, TEM, and HR-TEM. The size of the NiO nanoparticles obtained from the PSP-4-PVP (polyvinylpyrrolidone) precursors inside the different matrices follow the order of SiO_2 > TiO_2 > Al_2O_3. However, NiO nanoparticles obtained from the chitosan precursor does not present an effect on the particle size. It was found that the medium effect of the matrices (SiO_2, TiO_2, Al_2O_3, and $Na_{4.2}Ca_{2.8}(Si_6O_{18})$) on the photocatalytic methylene blue degradation, can be described as a specific interaction of the NiO material acting as a semiconductor with the M_xO_y materials through a possible p-n junction. The highest catalytic activity was found for the TiO_2 and glass composites where a favorable p-n junction was formed. The isolating character of Al_2O_3 and SiO_2 and their non-semiconductor behavior preclude this interaction to form a p-n junction, and thus a lower catalytic activity. NiO/SiO_2 and NiO/$Na_{4.2}Ca_{2.8}(Si_6O_{18})$ showed a similar photocatalytic behavior. On the other hand, the effect of the matrix on the optical properties for the NiO/SiO_2, NiO/TiO_2, NiO/Al_2O_3, and NiO/$Na_{4.2}Ca_{2.8}(Si_6O_{18})$ composites can be described by the different dielectric constants of the SiO_2, TiO_2, Al_2O_3, $Na_{4.2}Ca_{2.8}(Si_6O_{18})$ matrices. The maxima absorption of the composites (λ_{max}) exhibit a direct relationship with the dielectric constants, while their semiconductor bandgap (E_g) present an inverse relationship with the dielectric constants. A direct relationship between λ_{max} and E_g was found from these correlations. The effect of the polymer precursor on the particle size can explain some deviations from this relationship, as the correlation between the particle size and absorption is well known. Finally, the NiO/$Na_{4.2}Ca_{2.8}(Si_6O_{18})$ composite was reported in this work for the first time.

Keywords: nickel oxide; photocatalysis; chitosan; polyvinylpyrrolidone; optical properties

1. Introduction

Metal oxide nanoparticles are widely used in many applications such as coatings, catalysis, electrode materials, or sensors [1]. It is important to remark that their physical and chemical properties are strongly influenced by their agglomeration [2]. In this sense, it is well known that the incorporation of metal oxides onto inert support materials with high surface areas could help prevent particle agglomeration and also improve their reactivity and stability [3,4].

NiO is a p-type semiconductor with E_G = 3.5 eV presenting multiple practical applications [4–6]. However, their band gap can be modified by doping with other metal oxide semiconductors, and thus changing their photocatalytic properties [5,6]. NiO has been widely used in catalysis, battery cathodes, fuel cell electrodes, electrochromic films, electrochemical supercapacitors, or magnetic materials [4–6]. In this sense, Bonomo et al. [7] recently reported on the electrochemical and opto-electrochemical properties of nanostructured NiO for photoconversion applications. Although these applications are determined by their band-gap, which depend on the environment [8,9], no systematic studies have been reported regarding the effect of the medium on the band-gap behavior [10–12]. In this sense, it is well known that the dielectric medium affects the optical properties of nanoparticles, as previously observed for Au and Ag systems [10]. The optical properties of Au nanoparticles embedded into TiO_2, ZrO_2, and Al_2O_3 have been also studied qualitatively [10]. In addition, the effect of SiO_2, TiO_2, and ZrO_2 supports was recently analyzed showing that MoO_3/SiO_2 is the most efficient epoxidation catalyst [12].

The $Na_{4.2}Ca_{2.8}(Si_6O_{18})$ compound (combeite) is a crystalline phase normally obtained from the fusion of precursor $Na_2O{\cdot}CaO{\cdot}SiO_2$ glasses [13–15]. In this sense, there are no reported metal oxides using $Na_{4.2}Ca_{2.8}(Si_6O_{18})$ as a solid matrix.

In previous works, we have reported a method to prepare metal and metal oxide nanostructured materials from a thermal treatment of the Chitosan $(ML_n)_x$ and PS-co-4-PVP $(ML_n)_x$ macromolecular complexes [16–18]. The method consists of two steps: (1) Formation of both macromolecular complexes by a solvent assisted reaction between the respective polymer and the metallic salt; and (2) a thermal process of the solid under air atmosphere.

The M° and M_xO_y nanostructures can be easily incorporated into SiO_2 matrices using a similar approach by different thermal treatments of the solid-state precursors: Chitosan $(ML_n)_x//SiO_2$ and PS-co-4-PVP $(ML_n)_x//SiO_2$ affording $M_xO_Y//SiO_2$ composites [19,20]. This method can be also used to prepare $NiO//M_xO_y$ composites using SiO_2, TiO_2, Al_2O_3, or $Na_{4.2}Ca_{2.8}(Si_6O_{18})$ matrices. Although a few methods were proposed to prepare NiO/SiO_2 [4,21,22], NiO/TiO_2 [6,23–25], NiO/Al_2O_3 [26–29] composites, none of them is as general and simple as the one described here. As for the $Na_{4.2}Ca_{2.8}(Si_6O_{18})$ case, although this particular composition has not been reported, similar nickel oxide doped with silica matrices have been successfully synthesized via a sol–gel process [30]. Furthermore, this solid state method has been used for other systems [31]. A summary of the proposed fabrication route is shown in Figure 1 [13].

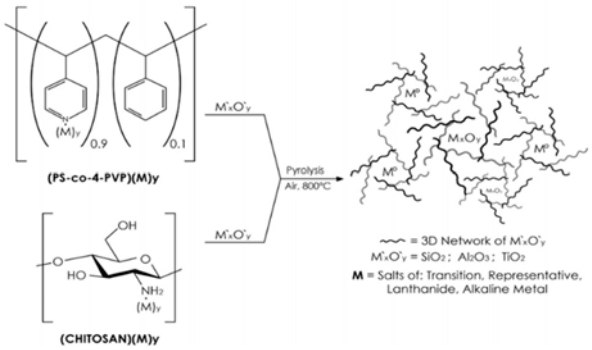

Figure 1. Schematic representation of the preparation method of metallic M° and metal oxides M_xO_y nanoparticles inside $M'_xO'_y$ matrices.

In addition, the effect of the different matrices on the optical properties will also be studied and discussed.

2. Materials and Methods

$NiCl_2{\cdot}6H_2O$, tetraethyl orthosilicate (TEOS), chitosan, poly(styrene-*co*-4-vinilpyridine) PS-co-4-PVP, ethyl alcohol, acetic acid, and dichloromethane were supplied from Sigma-Aldrich and were used as received.

2.1. Preparation of the NiO/SiO_2, NiO/TiO_2, NiO/Al_2O_3 Composites

SiO_2 was prepared according to the literature procedures [19,20]. Briefly, tetraethoxysilane (TEOS), ethanol, and acetic acid were mixed in a molar ratio of 1:4:4 with water (nanopure milli-Q), and added over the dichloromethane solution of the previously prepared chitosan $(NiCl_2{\cdot}6H_2O)_x$ and PS-co-4-PVP $(NiCl_2{\cdot}6H_2O)_x$. The mixture was stirred for 3 days. The obtained gel was dried at 100 °C under a vacuum. The chitosan $(NiCl_2{\cdot}6H_2O)_x//SiO_2$ and PS-co-4-PVP $(NiCl_2{\cdot}6H_2O)_x//SiO_2$ precursors were finally calcined at 800 °C for 2 h under air.

2.2. Preparation of the Chitosan $(NiCl_2{\cdot}6H_2O)_x//TiO_2$ and PS-co-4-PVP $(NiCl_2)_x//TiO_2$ Precursors

TiO_2 was prepared according to the literature procedures [19,20]. Briefly, titanium tetra-isopropoxide ($Ti(OC_3H_7)_4$, TTIP) ethanol and acetic acid were mixed in a molar ratio of 1:4:4 with water (nanopure milli-Q), and added over the dichloromethane solution of the previously prepared chitosan $(NiCl_2{\cdot}6H_2O)_x$ and PS-co-4-PVP $(NiCl_2{\cdot}6H_2O)_x$. The mixture was stirred for 3 days. The obtained gel was dried at 100 °C under a vacuum. The solid chitosan $(NiCl_2{\cdot}6H_2O)_x//TiO_2$ and PS-co-4-PVP $(NiCl_2{\cdot}6H_2O)_x//TiO_2$ precursors were calcined at 800 °C for 2 h under air.

2.3. Preparation of the Chitosan $(NiCl_2{\cdot}6H_2O)_x//Al_2O_3$ and PS-co-4-PVP $(NiCl_2)_x//Al_2O_3$ Precursors

Al_2O_3 was prepared according to the literature procedures [27–30]. Briefly, $AlCl_3$, ethanol, and acetic acid were mixed in a molar ratio of 1:4:4 with water (nanopure milli-Q), and added over the dichloromethane solution of the previously prepared chitosan $(NiCl_2{\cdot}6H_2O)_x$ and PS-co-4-PVP $(NiCl_2{\cdot}6H_2O)_x$. The mixture was stirred for 3 days. The obtained gel was dried at 100 °C under a vacuum. The solid chitosan $(NiCl_2{\cdot}6H_2O)_x//Al_2O_3$ and PS-co-4-PVP $(NiCl_2{\cdot}6H_2O)_x//Al_2O_3$ precursors were calcined at 800 °C for 2 h under air.

2.4. Preparation of the Precursors: Chitosan $(NiCl_2{\cdot}6H_2O)_x//NiO/Na_{4.2}Ca_{2.8}(Si_6O_{18})$ and PS-co-4-PVP $(NiCl_2)_x//NiO/Na_{4.2}Ca_{2.8}(Si_6O_{18})$

The compounds were prepared according to the literature procedures [28]. Briefly, tetraethoxysilane (TEOS), ethanol, and acetic acid were mixed in a molar ratio of 1:4:4 with water (nanopure milli-Q), then Na_2O, CaO, and SiO_2 solids (in mol% of 14:1.5:73) were added over the dichloromethane solution of the previously prepared chitosan $(NiCl_2{\cdot}6H_2O)_x$ and PS-co-4-PVP $(NiCl_2{\cdot}6H_2O)_x$. The mixture was stirred for 3 days. The obtained gel was dried at 100 °C under a vacuum. The solid chitosan $(NiCl_2{\cdot}6H_2O)_x//Na_2O\ CaO\ SiO_2$ and PS-co-4-PVP $(NiCl_2{\cdot}6H_2O)_x//Na_2O\ CaO\ SiO_2$ precursors were calcined at 800 °C for 2 h under air.

The coordination of the polymer was confirmed by IR analysis, as the broad ν(OH)+ ν(NH) band observed at 3448 cm^{-1} for free chitosan becomes unfolded upon coordination, shifting in the range of 3345–3393 cm^{-1}. On the other hand, the ν(py) band is shifting to high frequencies upon coordination [16–18].

Finally, polymer-metal complexes were placed into a box furnace (lab tech) using a pyrolysis temperature of 180 °C for the precursor complexes and 800 °C for the polymer complexes. Additional experimental conditions are summarized in Table 1.

Table 1. Composition of the pyrolytic products from the respective precursors.

Precursor	Precursor Formula	Matrix	Composite	Composite Number
(1)	Chitosan·$NiCl_2$ (chitosan)	-	NiO	C_1
(2)	PSP-4-PVP·$NiCl_2$ (PVP)	-	NiO	C_2
(3)	Chitosan·$NiCl_2$	SiO_2	NiO/SiO_2	C_3
(4)	PSP-4-PVP·$NiCl_2$	SiO_2	NiO/SiO_2	C_4
(5)	Chitosan·$NiCl_2$	TiO_2	NiO/TiO_2	C_5
(6)	PSP-4-PVP·$NiCl_2$	TiO_2	NiO/TiO_2	C_6
(7)	Chitosan·$NiCl_2$	Al_2O_3	NiO/Al_2O_3	C_7
(8)	Chitosan·$NiCl_2$	$Na_{4.2}Ca_{2.8}(Si_6O_{18})$	NiO/$Na_{4.2}Ca_{2.8}(Si_6O_{18})$	C_8

2.5. Characterization

IR spectra were recorded with a FT-IR Jasco 4600 spectrophotometer (Jasco Inc., Easton, MD, USA). Scanning electron microscopy (SEM) was performed on a JEOL 5410 scanning electron microscope (JEOL Ltd., Tokyo, Japan). Elemental microanalysis was performed by energy dispersive X-ray (EDS) analysis using a NORAN Instrument micro-probe attached to the SEM (Thermo Scientific, Waltham, MA, USA). High-resolution transmission electron microscopy (HR-TEM) was performed using a JEOL 2000FX TEM microscope (JEOL Ltd., Tokyo, Japan)at 200 kV to characterize the average particle size, distribution, and elemental and crystal composition. EDS analysis was performed in individual particles in order to discriminate NiO from the matrix. Average particle sizes were calculated using the Digital Micrograph software (Gatan, Inc., Pleasanton, CA, US). Methylene blue (MB) was used as a model compound to test the photocatalytic properties at 655 nm under UV-Vis illumination (Shimadzu UV-2600 spectrophotometer, Shimadzu Coorporation, Kyoto, Japan) using a xenon lamp (150 W) positioned 20 cm away from the photoreactor in a 330–680 nm range at room temperature, to avoid the self-degradation and thermal catalytic effects of cationic dye. Suspensions were stirred in the dark for 60 min to establish an adsorption/desorption equilibrium, after which the photocatalytic discoloration of MB was initiated.

3. Results and Discussion

3.1. Composite NiO/SiO_2

The X-ray diffraction pattern of the as-synthesized NiO/SiO_2 composite for the material from the chitosan precursor is shown in Figure 2a. All the reflection peaks of the XRD pattern can be indexed to NiO and SiO_2 phases [19] (JPDS no. 03-065-2901 for NiO and JPDS no. 01-088-1535 for SiO_2). The broad feature appearing at 22° corresponds to amorphous silica [19]. Similar X-ray diffraction patterns for NiO from the PVP precursor were obtained.

The SEM analysis (Figure 2b) shows irregular particle agglomerates, as typically observed from the preparation of nanoparticles using the solid-state thermal route [30]. From the TEM analysis, the agglomeration of NiO nanoparticles embedded into a mesh of SiO_2 can be observed in Figure 2c, where these agglomerates are composed of fused NiO nanoparticles. The size of these nanoparticles are in the range of 14 nm with a mean size of 25 nm (Figure 2c). Detailed HR-TEM images in Figure 2e,f show a homogeneous dispersion of NiO over the silica network. However, it was not possible to acquire high resolution images in order to study the interfaces between NiO and the different matrices. In any case, as also confirmed by SEM-EDS mapping (Figure 2g), there is a uniform distribution of NiO and SiO_2 particles. Similar results were observed for NiO obtained from the PVP precursor (see Supplementary Materials, Figure S1). The only difference is that NiO particles are bigger in size ca. 100 nm.

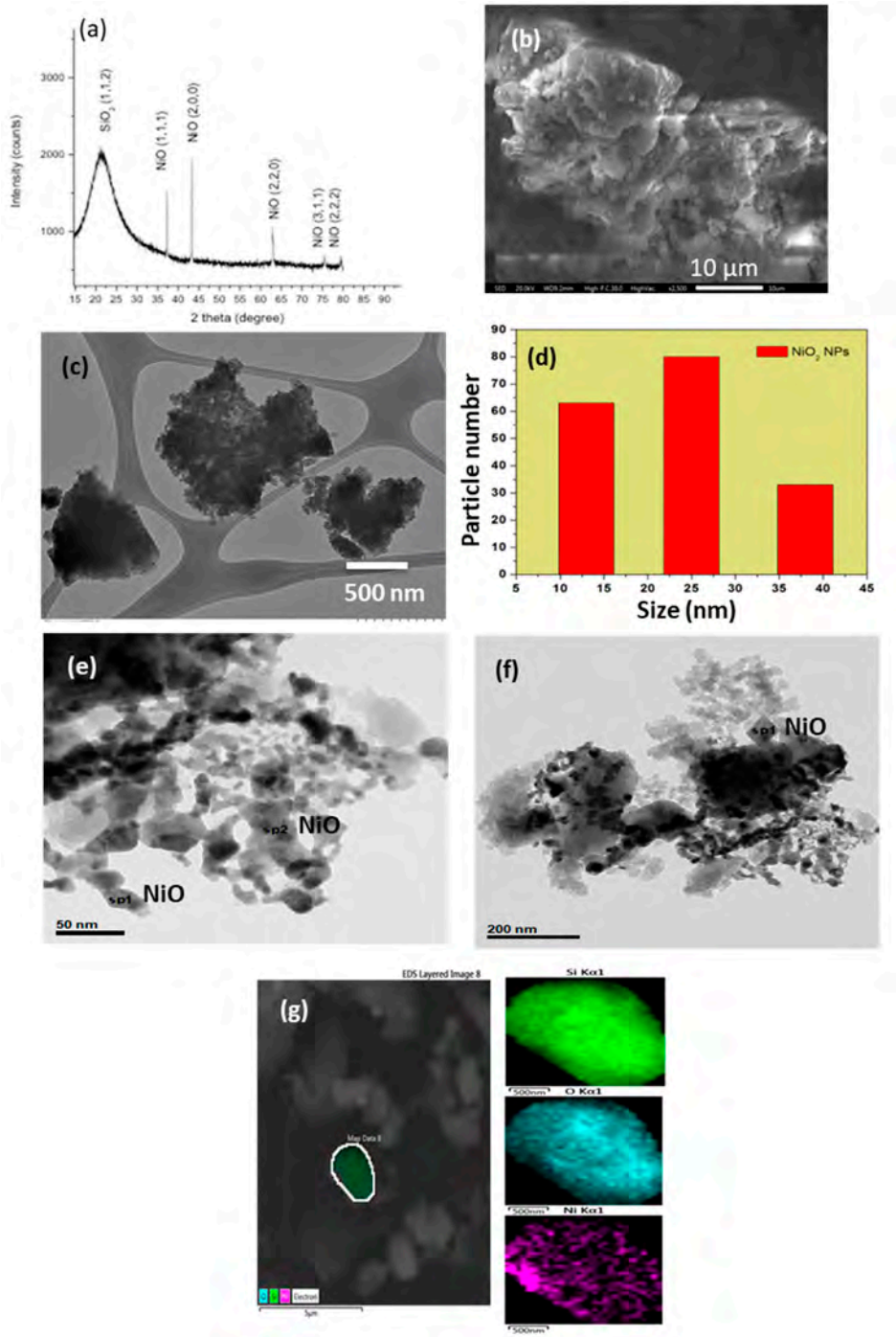

Figure 2. (**a**) XRD pattern; (**b**) SEM image; (**c**) TEM image; (**d**) particle histogram; (**e**,**f**) HRTEM images; and (**g**) SEM element mapping of the pyrolytic NiO compound obtained using the chitosan precursor.

3.2. NiO/TiO_2

Figure 3 shows the XRD pattern of the NiO/TiO_2 nanocomposite from the chitosan precursor, where the anatase phase and NiO are observed as single phases. Using this method, the pure TiO_2 anatase phase was obtained, in contrast with other solution methods, where a mixture of anatase and rutile in the NiO/TiO_2 composite was obtained [22]. The NiO/TiO_2 composite shows a "cotton" type morphology from the chitosan precursor (Figure 3b), whereas the morphology from the PVP precursor presents a more densified structure, as shown in Figure 3c. The SEM-EDS mapping, shown in

Figure 2g, indicates an homogeneous distribution of NiO and TiO_2. Similar results were obtained for the NiO/TiO_2 from the PVP precursor (see Supplementary Materials, Figure S2).

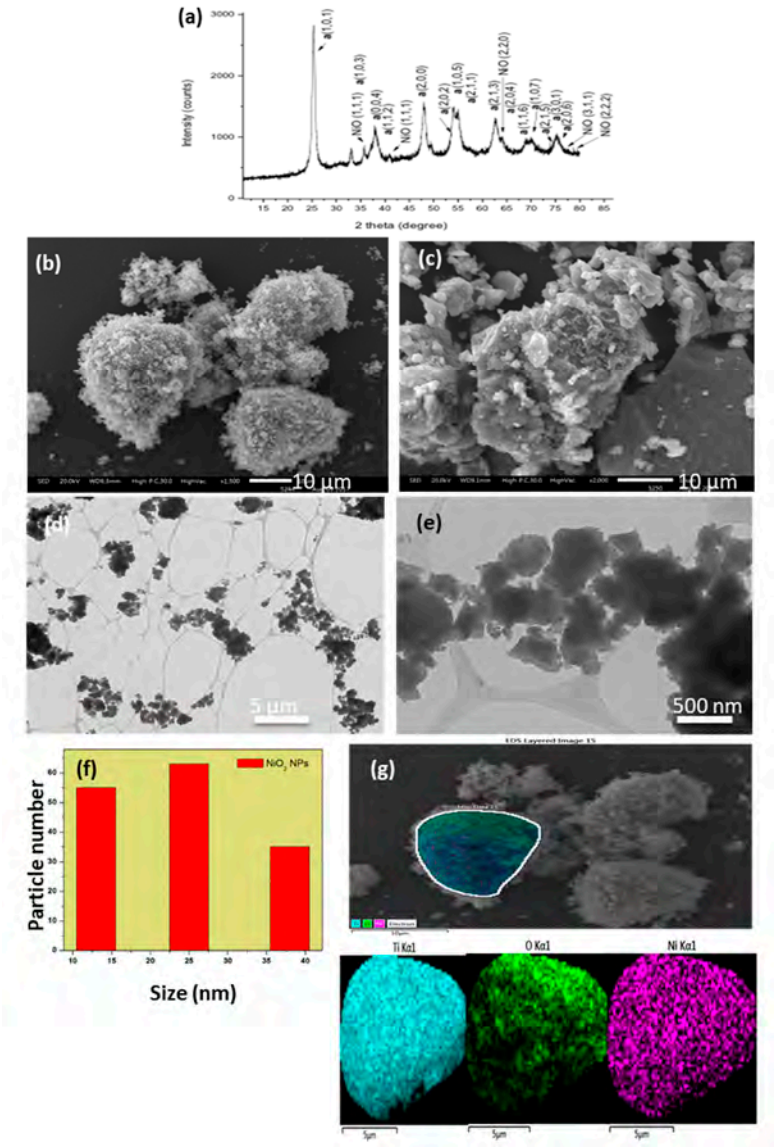

Figure 3. (**a**) XRD pattern; (**b**) SEM image of NiO from chitosan and (**c**) from PVP; (**d**,**e**) TEM images of NiO from chitosan and (**f**) their histogram; and (**g**) SEM mapping element for NiO from the chitosan precursor.

The TEM analysis (Figure 3d,e) presents a "spider web" TiO_2 network where the NiO nucleates forming agglomerated nanoparticles. They present a mean particle size of 25 nm (Figure 2f). A similar TEM analysis was observed for NiO/TiO_2 obtained from the PVP precursor (Figure 3b and Supplementary Materials, Figure S2).

3.3. NiO/Al_2O_3

Figure 4a shows the XRD pattern of the NiO/Al_2O_3 composite from the chitosan precursor where the corresponding peaks of γ-Al_2O_3 and NiO can be observed.

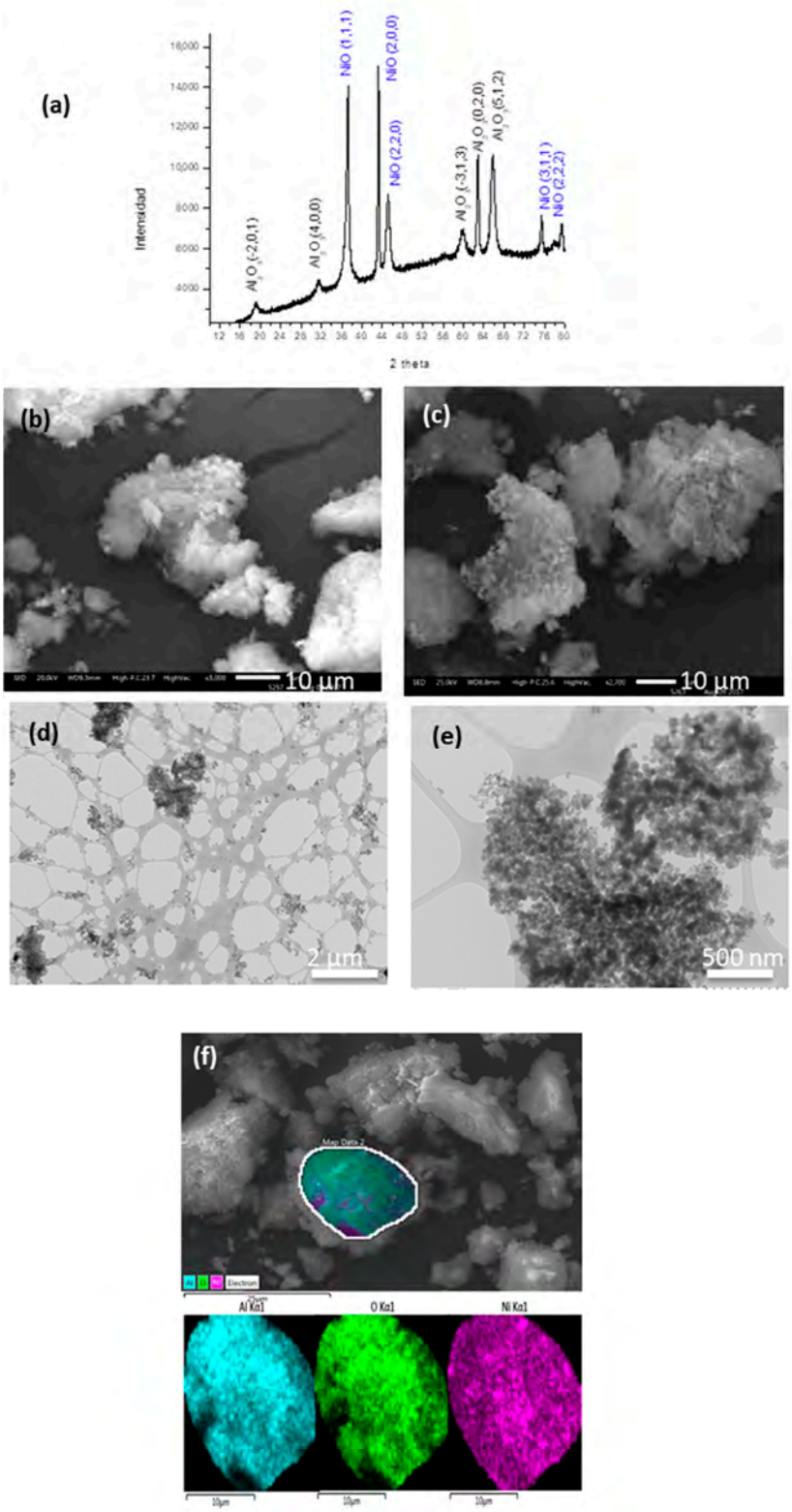

Figure 4. (**a**) XRD pattern of NiO/Al_2O_3 from the chitosan precursor; (**b**) SEM image of NiO from chitosan and (**c**) from PVP; (**d**) TEM image of NiO from chitosan and (**e**) from PVP; (**f**) EDS mapping of NiO from chitosan.

The effect of the polymer template on the morphology can be observed in Figure 4b,c. The chitosan precursor induces a "cotton" type morphology, while the PVP precursor also combines dense and

irregular zones. Figure 4f shows an elemental mapping image demonstrating that NiO is well dispersed inside Al_2O_3. A complete characterization is shown in Supplementary Materials, Figure S3.

As observed for the NiO/TiO_2 system, the TEM analysis (Figure 4e) shows a "spider web" network of Al_2O_3 where the NiO nucleates form agglomerates. The histogram (Supplementary Materials, Figure S3) shows a particle mean size of 17 nm. The HRTEM image of the NiO/Al_2O_3 from the PVP precursor is shown in Supplementary Materials, Figure 3c, where it can be observed that the medium particle size is 32 nm.

3.4. NiO/$Na_{4.2}Ca_{2.8}(Si_6O_{18})$

The XRD pattern of the NiO/$Na_{4.2}Ca_{2.8}(Si_6O_{18})$ composite prepared from the chitosan precursor indicates the formation of NiO inside the glass $Na_{4.2}Ca_{2.8}(Si_6O_{18})$ (see Figure 5a). The XRD pattern is in agreement with those reported in the literature [13–15]. The observed morphology is similar to the one previously reported [13–15] (see Figure 5b,c), also presenting a uniform distribution of NiO inside the $Na_{4.2}Ca_{2.8}(Si_6O_{18})$ (Figure 5d). Similar conclusions can be deduced for the PVP precursor (see Supplementary Materials, Figure S4).

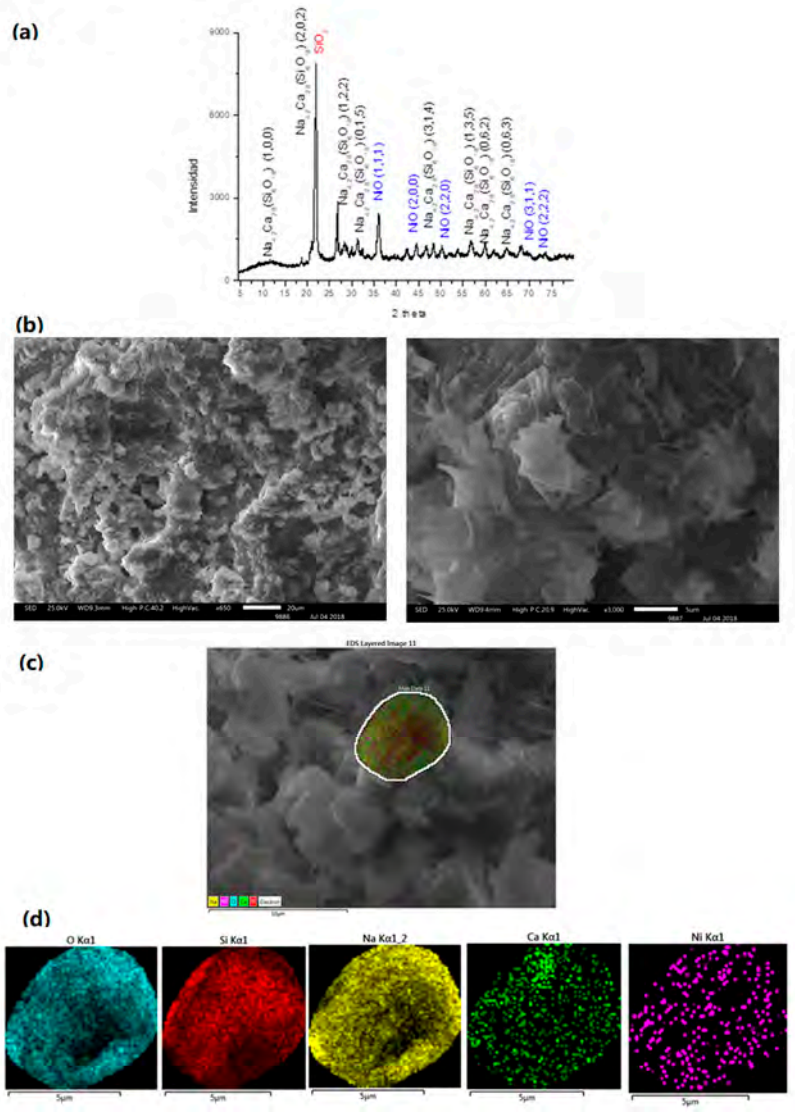

Figure 5. (**a**) XRD pattern of NiO inside $Na_{4.2}Ca_{2.8}$ (Si_6O_{18}); (**b**) and (**c**) SEM images; and (**d**) EDS mapping by an element of the composite NiO/$Na_{4.2}Ca_{2.8}(Si_6O_{18})$.

A summary of the medium particle sizes for NiO included into the different matrices is presented in Table 2, where the effect of the matrix and that of the polymer precursors on the final particle sizes can be observed.

Table 2. Nanoparticle size for the composites.

Composite	Precursor Formula	Particle Size (nm)	Reference
NiO	Chitosan·$NiCl_2$	>50	[17]
NiO	PSP-4-PVP·$NiCl_2$	>50	[17]
NiO/SiO_2	Chitosan·$NiCl_2$	25	This work
NiO/SiO_2	PSP-4-PVP·$NiCl_2$	100	This work
NiO/TiO_2	Chitosan·$NiCl_2$	25	This work
NiO/TiO_2	PSP-4-PVP·$NiCl_2$	63	This work
NiO/Al_2O_3	Chitosan·$NiCl_2$	30	This work
NiO/Al_2O_3	Chitosan·$NiCl_2$	17	This work
NiO/$Na_{4.2}Ca_{2.8}(Si_6O_{18})$	Chitosan·$NiCl_2$	Not measured	This work

The nanoparticle size of NiO obtained from the PVP precursor inside the matrices follow the order of SiO_2 > TiO_2 > Al_2O_3, while that for the NiO from the chitosan precursor does not present a significant effect on the nanoparticle size.

3.5. Photocatalytic Behavior

Although the main applied property of NiO is in the field of electrochemistry as Li-ion batteries [32] and supercapacitors applications, [33] its application as a photocatalytic activity toward organic dyes have also been suggested [34]. In any case, reports on the photocatalytic activity toward organic dyes using NiO/matrices are scarce. Yu et al. [6] found a higher photocatalytic activity for NiO/TiO_2 than for pure NiO, towards the photodegradation of p-chlorophenol. Regarding the photocatalytic efficiency when using composites, important parameters to be considered include the formation of hierarchical porous structures, the dispersion of the catalytic semiconductor on the matrix surface, and the p-n junction in a NiO/M_xO_y composite, where a new band gap will be formed with a most favorable value for the photodegradation chemical processes.

3.6. NiO

Methylene blue (MB) is extensively used as an organic dye in coloring paper, temporary hair colorant, dyeing cottons, and coating for paper stock [35]. The removal of this hazardous dye is considered as one of the growing requirements in recent years. The photocatalytic experiments were carried on the sample with definite dye concentration under dark conditions and UV irradiation. The band-gap of the NiO is 5.0 and 5.2 eV, when it is prepared from chitosan and PVP precursors, respectively. For the semiconductor metal oxides, their band gap value dictates their photocatalytic activity [35,36]. For this reason, the band gap of the C_3–C_8 composites was determined. These values are: 5.0, 5.2, and 5.4 eV for the NiO/SiO_2, NiO/TiO_2, NiO/Al_2O_3 composites, respectively, all obtained from the chitosan precursors. The values for the PVP precursor are: 5.5 eV, 5.2 eV for the NiO/SiO_2, NiO/TiO_2 composites, respectively. Those values do not change significantly, and are slightly higher than those reported previously, which can be due to their bigger particle sizes [34] (see Supplementary Materials, Figure S5).

The changes in the absorption spectra of the MB aqueous solution exposed to UV light for various times in the presence of NiO are shown in Supplementary Materials, Figure S6. The peak at 655 nm is characteristic of methylene blue and decreases with the irradiation time. Figure 6 shows the plot of time vs. concentration of methylene blue measured as C/C_o for NiO arising from both

precursors, obtaining a catalytic efficiency of ~68% and ~71% of degradation in 5 h (see Figure 6c). Both degradation processes follow a zero order, as shown in Figure 6b,d. As previously mentioned, only a few photodegradation studies for NiO have been reported. For example, using 3 nm NiO nanoparticles [34] and NiO nanofibers [5], a moderated catalytic activity towards Rhodamine B was observed. In both cases, the degradation kinetic was zero order, which means that the rate of degradation does not depend on the MB concentration. This type of model is normally observed when the surface of the photocatalyst is saturated with the dye, so that the degradation rate remains relatively constant, depending only on the generation of photo-induced charges in the catalyst.

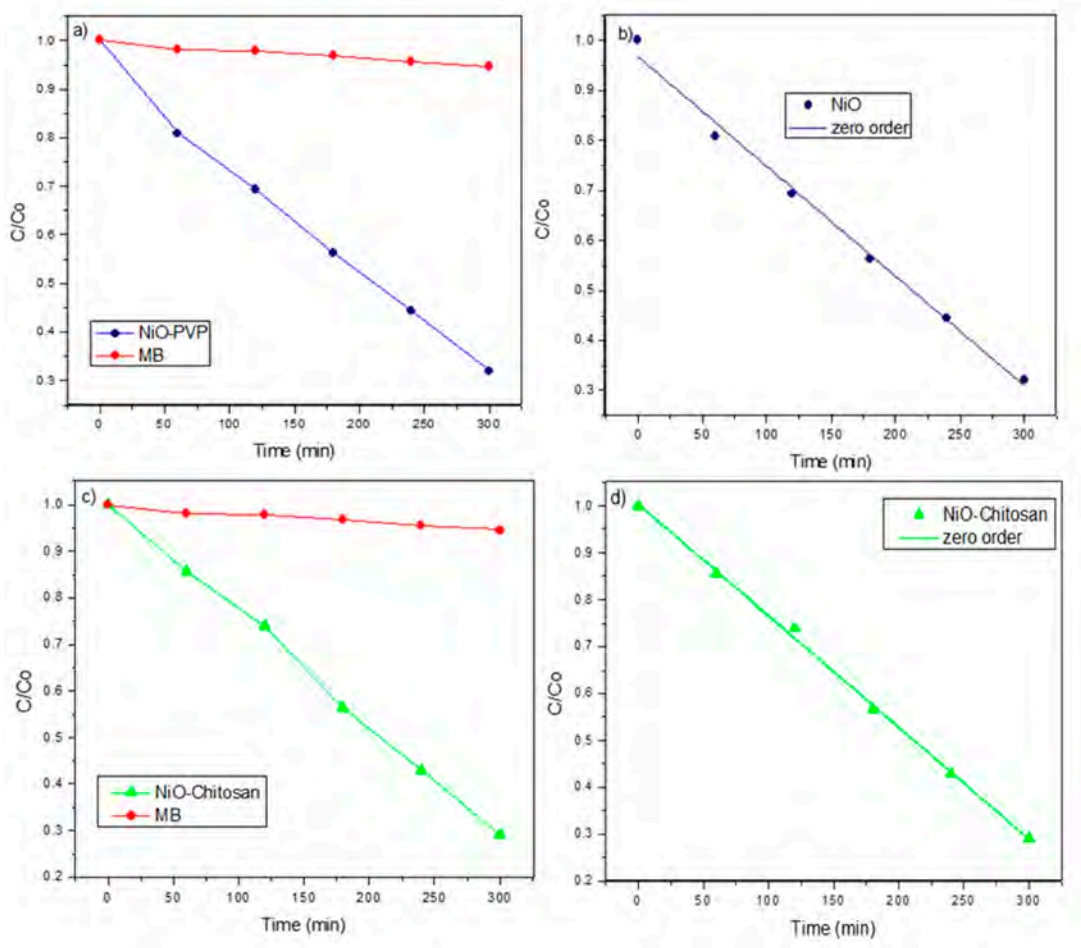

Figure 6. (**a**) Normalized concentration changing of methylene blue (MB) without the catalyst and in the presence of NiO from the PVP and (**b**) their zero order kinetic of degradation of MB, (**c**) changing of MB without the catalyst and in the presence of NiO from the chitosan and (**d**) their zero order kinetic of MB degradation.

3.7. NiO in Matrices

The photocatalytic activity towards MB degradation for the NiO composite using different matrices is shown in Figure 7. The degradation rate of the NiO/TiO_2 composite is shown for comparison. In any case, the photocatalytic activity of these NiO compounds is still far from the pure TiO_2 standard phase [37]. For example, we have recently reported a 98% discoloration rate in only 25 min for TiO_2 nanostructures using similar synthetic routes, and the degradation of commercial TiO_2 (Degussa P25) is about 75% of MB under the same experimental conditions [38]. A representative plot of MB absorption at 655 nm vs. time is given in Supplementary Materials, Figure S6. A summary of the kinetic degradation data is also displayed in Table 3.

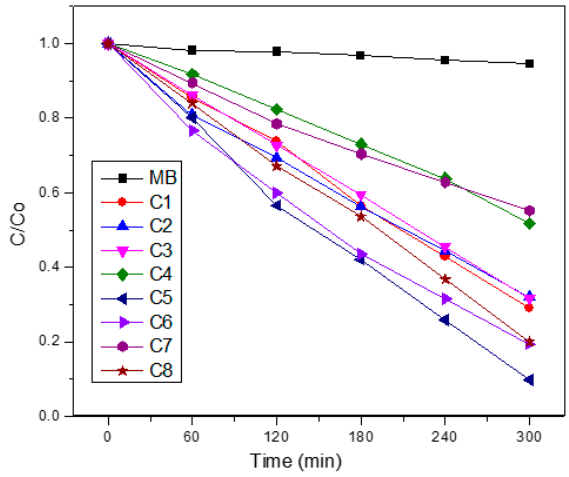

Figure 7. Photocatalytic behavior of NiO embedded in several matrices.

Table 3. Kinetic data for the photodegradation process of MB with NiO and NiO/SiO_2, NiO/TiO_2, NiO/Al_2O_3, and NiO/$Na_{4.2}Ca_{2.8}(Si_6O_{18})$ composites.

Photocatalyst	Apparent Photodegradation *	Discoloration Rate (%)	R^2 Linear Fit (%)
NiO-CHITOSAN	2.4	71%	0.998
NiO-PS-4-PVP	2.2	68%	0.991
NiO/SiO_2-CHITOSAN	2.3	69%	0.999
NiO/SiO_2-PS-4-PVP	1.6	48%	0.996
NiO/TiO_2 -CHITOSAN	2.9	91%	0.992
NiO/TiO_2-PS-4-PVP	2.6	81%	0.980
NiO/Al_2O_3-CHITOSAN	1.5	45%	0.990
NiO/$Na_{4.2}Ca_{2.8}(Si_6O_{18})$	2.6	75%	0.990

* Rate constant k (10^{-3} M·min^{-1}).

As seen in Figure 6, the NiO from the chitosan precursor produces a higher activity than that arising from the PVP precursor. These results also apply for both SiO_2 and TiO_2 matrices. Interestingly, the most efficient photocatalytic activity was observed for the NiO/TiO_2 composite with a 91% degradation of methylene blue in 5 h. This can be probably related with a matrix effect of SiO_2, TiO_2, and Al_2O_3.

Our results of catalytic degradation for the NiO//TiO_2 composite (about 91%) are similar or slightly higher than those reported in the literature. Ahmed claimed 90% of catalytic degradation efficiency on the NiO//TiO_2 composite prepared from titanium chloride and nickel acetylacetonate [39]. Faisal et al. obtained a similar catalytic degradation efficiency using an ultrasonication method [40]. Sim et al. reported 86% of the degradation efficiency using plasma enhanced chemical vapor deposition (PECVD) with hydro-oxygenated amorphous titanium dioxide obtained from titanium tetra-isopropoxide [Ti(OC3H7)4, TTIP] liquid as a precursor [41]. Finally, Chen et al. reported 86% catalytic degradation of MB using a method that involves incipient wet impregnation of the nickel oxide (NiO) nanoparticles over previously prepared TiO_2 nanotubes [24].

It is suggested that for the most catalytically active TiO_2 as the matrix, a p-n junction can be formed acting NiO as p-NiO and TiO_2 as n-TiO_2, see Supplementary Materials, Figure S7, leading to a reduction of the recombination rate of photogenerated electron-hole pairs, which is known to enhance the photocatalytic activity of TiO_2. A detailed description of the mechanism can be found on Supplementary Materials, Figure S8. Therefore, it seems that the matrix is playing a crucial role for the NiO/TiO_2 composite and in this case, the NiO acts as the matrix rather than an active semiconductor.

On the other hand, the less efficient photocatalyst toward MB degradation arises probably from an insulating Al_2O_3 effect [28,42], which preclude the p-NiO behavior. This is in agreement with the observed photocatalytic decrease for the TiO_2/SiO_2 composite in comparison with pure TiO_2. In the case of the NiO/SiO_2 composite, the lower photocatalytic activity is probably a consequence of the high porous morphology which is induced by the SiO_2 matrix. All the photodegradation processes of MB with NiO/SiO2, NiO/TiO_2, NiO/Al_2O_3, and $NiO/Na_{4.2}Ca_{2.8}(Si_6O_{18})$ composites exhibited a zero order kinetic law, as shown in Supplementary Materials, Figure S9.

3.8. Photocatalytic Activity of the NiO/$Na_{4.2}Ca_{2.8}(Si_6O_{18})$ Composite

The photocatalytic activity of the $NiO/Na_{4.2}Ca_{2.8}(Si_6O_{18})$ composite obtained from the chitosan precursor is shown in Figure 7 and the kinetic data is also shown in Table 2. It is observed that the photocatalytic activity is higher than that of NiO, NiO/SiO_2, and NiO/Al_2O_3 but lower than of NiO/TiO_2. It is concluded that the $Na_{4.2}Ca_{2.8}(Si_6O_{18})$ sample presents a similar behavior to those of the SiO_2 sample.

3.9. Effect of the Matrices on λ_{max} and E_g

Figure 8 shows the variation of both E_g and λ_{max} for the different matrices. The respective UV-Vis absorption spectra of the composites are shown in Supplementary Materials, Figure S9. The band-gap values were estimated from these spectra using the Tauc procedure (Supplementary Materials, Figure S9). Considering that the static dielectric constants (K) for the matrices are: SiO_2 3.9; TiO_2 80, and Al_2O_3 8.8 [43], both E_g and λ_{max} could be related to the dielectric constant of the matrix. Unfortunately, there is no available data for $Na_{4.2}Ca_{2.8}(Si_6O_{18})$. The dependence of E_g with the dielectric constant ε is not totally understood, where several relationships have been previously found [43–45]. The shape of the experimental or theoretical expression depends, among others, on the type of materials. On the other hand, the relationship of λ_{max} with ε and the refractive index n is known for metallic nanoparticles [8]:

$$\lambda_{max} \propto \lambda_p \sqrt{2\varepsilon + 1} \cong \sqrt{2}\, \lambda_p\, n \quad (1)$$

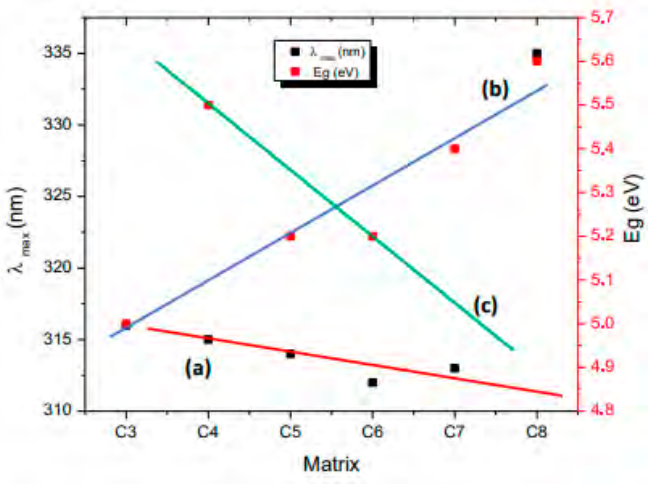

Figure 8. Variation of both E_g and λ_{max} with the different matrices.

However, the analogue relationship for metal oxides is not completely understood. The plot of λ_{max} for the NiO vs. the refractive index [46,47] for the SiO_2, TiO_2, and Al_2O_3 matrices shows an inverse and irregular relationship (see Supplementary Materials, Figure S10). Then, according to Figure 8, the variations of E_g and λ_{max} can be explained by a physical effect of the medium reflected in their dielectric constant of the different matrices. A close inspection of Figure 8 suggests the presence

of three linear trends. In Figure 8, it can be observed that λmax varied inversely with the properties of the matrices (i.e., dielectric constant for instance) for the NiO obtained from both polymers in an approximate linear behavior. The composite C_8 having a "silica like" matrix does not follow this trend due to an unknown effect. Although the dependence of λmax with the dielectric or refractive index given by Equation (1) indicates a direct linear dependence, our results show an inverse linear trend. Then, the Equation (1) may not be valid for metallic oxides. A new equation is proposed (Equation (2), curve a in Figure 8), which could arise from the general trends for nanostructured metallic oxides. This is consistent with the fact observed in Supplementary Materials, Figure S9, where an inverse relationship of λmax with n is shown.

In addition, Eg values vary in a direct or inverse way depending on the NiO polymer precursor (direct behavior for the chitosan; curve b, Equation (3) or inverse for the PVP precursor; curve c, Equation (4)). As previously mentioned, the dependence of E_g with the dielectric constant ε is not totally understood, and this is a matter of controversy in the literature. The inverse relationship (curve c) is in agreement with the results reported by Hervé and Vandamme [48], while the direct relationship (curve b) shows a similar trend to that shown by Kumar and Singh [49]. In any case, we do not have any clear explanation of the different dependencies of Eg with n and ε when using the different polymer precursors.

From the plot shown in Figure 8, the following equations can be established:

$$\lambda_{max} = a/(\varepsilon,n); \text{ valid for NiO from chitosan and PVP} \quad (2)$$

$$Eg = b/(\varepsilon,n); \text{ valid for NiO from chitosan} \quad (3)$$

$$Eg = c/(\varepsilon,n); \text{ valid for NiO from PVP} \quad (4)$$

The following equations are then obtained by combining both expressions:

$$Eg = ab/\lambda_{max}; \text{ valid for NiO from chitosan} \quad (5)$$

$$Eg = c\lambda_{max}/a; \text{ valid for NiO from PVP} \quad (6)$$

In agreement with these new expressions, we can explain the effect of the physical properties of the matrices on the band gap with the refraction index or the dielectric constant. The experimental data fits into these equations, as seen in Figure 9 plots d (Equation (5)) and e (Equation (6)). These equations describing the effect of the medium modulated by various solid matrices on the band gap and the maximum absorption could be valid for other nanostructured metal oxides included in solid matrices. In order to validate this, additional experiments with other systems are being carried out.

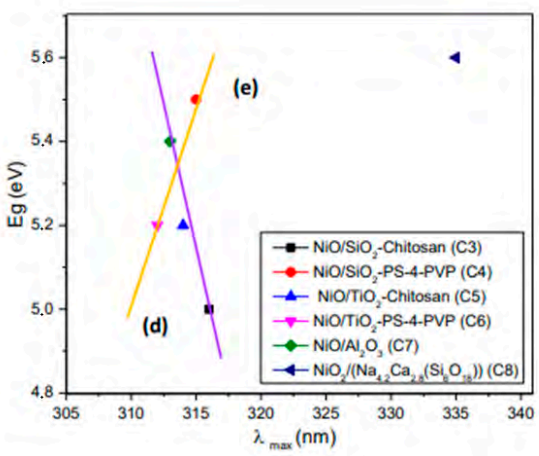

Figure 9. Relationship between E_g and λ_{max} for the composites the NiO/SiO_2, NiO/TiO_2, NiO/Al_2O_3, and $NiO/Na_{4.2}Ca_{2.8}(Si_6O_{18})$.

Experiments linking the band gap with the size and the maxima absorption of nanoparticles have been performed for other metal oxides such as ZnO [50,51], as well as for noble metal nanoparticles such as Au [52], Ag [32], and Pt [53]. However, there are no studies in the literature about the medium expressed by solid matrices on nanostructured metallic oxides.

4. Conclusions

NiO/SiO_2, NiO/TiO_2, NiO/Al_2O_3, and NiO/glass composites were satisfactorily prepared by a solid-state synthesis from the chitosan and PVP precursors. XRD, SEM/EDS, and HR-TEM were used to characterize the new formed composites. It was concluded that the nature of the precursor polymer influences the morphology, as well as the size of the obtained nanoparticles. The chitosan precursor induces the smallest NiO nanoparticles and also their respective nanocomposites. In addition, the nature of the matrix influences the NiO nanoparticle size, following the order of $SiO_2 > TiO_2 > Al_2O_3$ for the PVP precursor. However, no relationship on the particle size was observed for the NiO obtained from the chitosan precursor.

The efficiency on the photocatalytic activity depends on the formation of a p-n junction between NiO acting as p-NiO and the metal oxide matrix acting as n-metal oxide. TiO_2 presents the most effective p-NiO//n-TiO_2 junction. On the other hand, the optical parameters Eg and λ_{max} depends on the dielectric constant and the refractive index of the matrix medium in a manner which depends on the preparation procedure. The "silica like" $Na_{4.2}Ca_{2.8}(Si_6O_{18})$ matrix does not follow these correlations. New equations describing the effect of the physical properties (dielectric constant and the refractive index) are proposed, which could be used for other metal oxides included in solid matrices.

Supplementary Materials: The following are available online at http://www.mdpi.com/2079-4991/10/12/2470/s1, Figure S1: (**a**) SEM-EDS mapping by element and (**b**) TEM images and (**c**) HRTEM image of NiO from the PS-co-4-PVP $(NiCl_2)_x$ $//SiO_2$ precursor, Figure S2: (**a**) SEM-EDS mapping by element from the PS-co-4-PVP·$(NiCl_2)n)x//TiO_2$ precursor and (**b**) TEM images and its histogram of the pyrolytic product from the PS-co-4-PVP·($NiCl_2)n)x//TiO_2$ precursor, Figure S3: (**a**) SEM-EDS mapping by element and (**b)** TEM images, Histogram and electron diffractions, of the pyrolytic product from the precursor PS-co-4-PVP·$(NiCl_2)n)x$ $//Al_2O_3$ and (**c**) Histogram of TEM image of NiO from Chitosan·$(NiCl_2)n)x$ $//Al_2O_3$ precursor, Figure S4: SEM image and EDS mapping analysis for the composite $NiO/Na_{4.2}$ $Ca_{2.8}$ (Si_6O_{18}) from the PS-co-4-PVP·$(NiCl_2)n)//SiO_2$·CaO·Na_2O precursor, Figure S5: Tauc determination of Eg values for NiO from Chitosan·$(NiCl_2)n$. and PS-co-4-PVP·$(NiCl_2)n$ and for NiO/SiO_2, NiO/TiO_2, NiO/Al_2O_3 and $NiO/Na_{4.2}$ $Ca_{2.8}(Si_6O_{18})$ composites, Figure S6: Absorbance vs time for the blue methylene degradation for NiO (**a**) and for the composites NiO/SiO_2, NiO/TiO_2, NiO/Al_2O_3; (**b**) NiO/SiO_2 from Chitosan·$(NiCl_2)x//TiO_2$; (**c**) NiO/SiO_2 from PS-co-4-PVP·$(NiCl_2)x//TiO_2$; (**d**) NiO/TiO_2 from Chitosan·$(NiCl_2)x$ $//TiO_2$; (**e**) NiO/TiO_2 from PS-co-4-PVP·$(NiCl_2)x$ $//TiO_2$; (**f**) NiO/Al_2O_3 from Chitosan·$(NiCl_2)x$ $//Al_2O_3$; (**g**) NiO/ $Na_{4.2}$ $Ca_{2.8}$ (Si_6O_{18}) from Chitosan·$(NiCl_2)x$ // Na_2O·CaO·SiO_2, Figure S7: Schematic diagrams for (**a**) energy bands of p-NiO and TiO_2 before contact, (**b**) formation of p-n junction and its energy diagram at equilibrium and (**c**) transfer of holes from n-TiO2 to p-NiO under UV irradiation, Figure S8: The photodegradation mechanism of NiO/TiO2 composites, Figure S9: Kinetic plot of the blue methylene degradation with the composites NiO/SiO_2, NiO/TiO_2, NiO/Al_2O_3 and $NiO/Na_{4.2}Ca_{2.8}(Si_6O_{18})$, Figure S10: UV-Vis absorption spectra of the composites, Figure S11: Plot of λ_{max} for the NiO vs the refractive index for the matrices SiO_2, TiO_2 and Al_2O_3.

Author Contributions: C.D. and M.L.V. conceived the idea and designed the experiments. O.C.-V. and M.S. carried out the preparation of the nanoparticles and performed the experimental analysis. M.A.L.-B. performed the TEM experimental measurements and analysis. C.D., M.L.V., M.S., O.C.-V. and M.A.L.-B. analyzed the data and wrote the manuscript. All authors have read and agreed to the published version of the manuscript.

Funding: The authors acknowledge the Fondecyt Project 1160241 for financial support. MLB also acknowledges the project PID2019-107106RB-C32 funded by the Spanish Ministry of Science and Innovation. The use of Servicio General de Apoyo a la Investigación (SAI, University of Zaragoza) is finally acknowledged.

Conflicts of Interest: The authors declare no conflict of interest.

References

1. Fernandez-Garcia, E.; Martinez-Arias, A.; Hanson, J.C.; Rodriguez, J.A. Nanostructured oxides in chemistry: Characterization and properties. *Chem. Rev.* **2014**, *104*, 4063–4104. [CrossRef] [PubMed]
2. Srivastava, A.K. *Oxide Nanostructures, Growth, Macrostructures and Properties*; Pan Stanford Publishing: Singapore, 2014.

3. Liu, S.; Han, M.-Y. Silica-coated metal nanoparticles. *Chem. Asian J.* **2010**, *5*, 36–45. [CrossRef]
4. Sietsma, J.R.A.; Meeldijk, J.D.; Den Breejen, J.P.; Versluijs-Helder, M.; van Dillen, J.A.; De Jongh, P.E.; De Jong, K.P. The Preparation of Supported NiO and Co_3O_4 Nanoparticles by the Nitric Oxide Controlled Thermal Decomposition of Nitrates. *Angew. Chem. Int. Ed.* **2007**, *46*, 4547–4549. [CrossRef] [PubMed]
5. Zhang, Z.; Shao, C.; Li, X.; Wang, C.; Zhang, M.; Liu, Y. Electrospun Nanofibers of p~Type NiO/n~Type ZnO Heterojunctions with Enhanced Photocatalytyc Activity. *ACS Appl. Mater. Interface Sci.* **2010**, *10*, 2915–2923. [CrossRef] [PubMed]
6. Yu, J.; Wang, W.; Cheng, B. Synthesis and Enhanced Photocatalytic Activity of a Hierarchical Porous Flowerlike p–n Junction NiO/TiO_2 Photocatalyst. *Chem. Asian* **2010**, *5*, 2499–2506. [CrossRef] [PubMed]
7. Bonomo, M.; Dini, D.; Decker, F. Electrochemical and Photoelectrochemical Properties of Nickel Oxide (NiO) with Nanostructured Morphology for Photoconversion Applications. *Front. Chem.* **2018**, *6*, 601. [CrossRef] [PubMed]
8. Jensen, T.R.; Duval, M.L.; Kelly, K.L.; Lazarides, A.A.; Schatz, G.C.; Van Duye, R.P. Nanosphere Lithography: Effect of the External Dielectric Medium on the Surface Plasmon Resonance Spectrum of a Periodic Array of Silver Nanoparticles. *J. Phys. Chem.* **1999**, *103*, 9846–9853. [CrossRef]
9. Kelly, K.L.; Coronado, E.; Zhao, L.L.; Schatz, G. The optical properties of metal nanoparticles: The influence of size, shape, and dielectric environment. *J. Phys. Chem.* **2003**, *107*, 668–677. [CrossRef]
10. Prevel, B.; Palpant, B.; Lerme, J.; Pellarin, M.; Treilleux, M.; Saviot, L.; Duval, E.; Perez, A.; Broyer, M. Comparative Analysis of Optica Properties of Gold and Silver Clusters Embedded in Alumina Matrix. *NanoStructured Mater.* **1999**, *12*, 307–310. [CrossRef]
11. Matsuoka, J.; Yoshida, H.; Nasu, H.; Kamiya, K. Preparation of Gold Microcrystal-Doped TiO_2, ZrO_2 and Al_2O_3 Films through Sol-Gel Process. *J. Sol Gel. Tech.* **1997**, *9*, 145–155. [CrossRef]
12. Chandra, P.; Doke, D.S.; Unbarkar, S.D.; Biradar, A.V. One-pot synthesis of ultrasmall MoO_3 nanoparticles supported on SiO_2, TiO_2, and ZrO_2 nanospheres: An efficient epoxidation catalyst. *J. Mater. Chem. A* **2014**, *2*, 19056–19060. [CrossRef]
13. Soares, V.O.; Daguano, J.K.M.B.; Lombello, C.B.; Bianchin, O.S.; Gonçalves, L.M.G.; Zanotto Edgar, D. New sintered wollastonite glass-ceramic for biomedical applications. *Ceram. Int.* **2018**, *44*, 20019–20027. [CrossRef]
14. Volzone, C.; Stábile, F.M. Structural Changes by Thermal Treatment up to Glass Obtention of P_2O_5-Na_2O-CaO-SiO_2 Compounds with Bioglass Composition Types. *New J. Glass Ceram.* **2013**, *3*, 53–57. [CrossRef]
15. Martel Estrada, S.A.; Armendáriz, I.O.; Torres García, A.; Hernández, J.F.; Rodríguez, C.A. González Evaluation of In Vitro Bioactivity of 45S5 Bioactive Glass/Poly Lactic Acid Scaffolds Produced by 3D Printing. *Int. J. Compos. Mater.* **2017**, *7*, 144–149.
16. Diaz, C.; Barrientos, L.; Carrillo, D.; Valdebenito, J.; Valenzuela, M.L.; Allende, P.; Geaney, H.; O'Dwyer, C. Solvent-less method for efficient photocatalytic α-Fe_2O_3 nanoparticles using macromolecular polymeric precursors. *New J. Chem.* **2016**, *40*, 6768–6776. [CrossRef]
17. Diaz, C.; Valenzuela, M.L.; Laguna-Bercero, M.A.; Orera, A.; Bobadilla, D.; Abarca, S.; Peña, O. Synthesis and magnetic properties of nanostructured metallic Co, Mn and Ni oxide materials obtained from solid-state metal macromolecular complex precursors. *RSC Adv.* **2017**, *7*, 27729–27736. [CrossRef]
18. Díaz, C.; Valenzuela, M.L.; Laguna, A.; Lavayen, V.; Jimenez, J.; Power, L.; O'Dwyer, C. Metallophosphazene Precursor Routes to Solid-State Deposition of Metallic and Dielectric Micro- and Nanostructures on Si and SiO_2. *Langmuir* **2010**, *26*, 10223–10233. [CrossRef]
19. Díaz, C.; Valenzuela, M.L.; Segovia, M.; De la Campa, R.; Soto, A.P. Solution, Solid-State Two Step Synthesis and Optical Properties of ZnO and SnO Nanoparticles and Their Nanocomposites with SiO_2. *J. Clust. Sci.* **2018**, *29*, 251–266. [CrossRef]
20. Díaz, C.; Valenzuela, M.L.; Bobadilla, D.; Laguna-Bercero, M.A. Bimetallic Au//Ag Alloys inside SiO_2 using a solid-state method. *J. Clust. Sci.* **2017**, *28*, 2809–2815. [CrossRef]
21. Zong, J.; Zhu, Y.; Yang, X.; Li, C. Confined growth of CuO, NiO, and Co_3O_4 nanocrystals in mesoporous silica (MS) spheres. *J. Alloys Compd.* **2011**, *509*, 2970–2975. [CrossRef]
22. Shufu, C.; Sujuan, Z.; Wei, L.; Wei, Z. Preparation and activity evaluation of p-n junction photocatalyst NiO/TiO_2. *J. Hazard. Mater.* **2008**, *155*, 320–326. [CrossRef] [PubMed]

23. Yu, J.H.; Yang, H.; Jung, R.H.; Lee, J.W.; Boo, J.H. Hierarchical NiO/TiO2 composite structures for enhanced electrochromic durability. *Thin Solid Films* **2018**, *664*, 1–5. [CrossRef]
24. Chen, J.-Z.; Chen, T.-H.; Lai, L.-W.; Li, P.-Y.; Liu, H.-W.; Hong, Y.-Y.; Liu, D.-S. Preparation and Characterization of Suface Photocatalytic Activity with NiO/TiO_2 Nanocomposite Structure. *Materials* **2015**, *8*, 4273–4286. [CrossRef]
25. Wang, T.T.; Chiang, C.L.; Lin, Y.C.; Srinivasadesikan, V.; Lin, M.C.; Lin, Y.G. KSCN-activation of hydrogenated NiO/TiO_2 for enhanced photocatalytic hydrogen evolution. *Appl. Surf. Sci.* **2020**, *511*, 145548. [CrossRef]
26. Makhlouf, S.; AKhalil, K.M.S. Humidity sensing properties of NiO/Al_2O_3 nanocomposite materials. *Solid State Ion.* **2003**, *164*, 97–106. [CrossRef]
27. Rogojan, R.; Andronescu, E.; Ghitulica, C.; Vasile, B. Synthesis and Characterization of Alumina Nano-power Obtanined by Sol-Gel Method. *UPB Sci. Bull. Ser. B* **2011**, *73*, 67–76.
28. Adams, L.A.; Essien, E.R.; Shaibu, R.O.; Oki, A. Sol-Gel Synthesis of SiO_2-CaO-Na_2O-P_2O_5 Bioactive Glass Ceramic from Sodium Metasilicate. *New J. Glass Ceram.* **2013**, *3*, 11–15. [CrossRef]
29. Kamire, R.J.; Majewski, M.B.; Hoffeditz, W.L.; Ohelan, B.T.; Farha, O.K.; Hupop, J.T.; Wasielewski, M.R. Photodriven hydrogen evolution by molecular catalysts using Al_2O_3-protected perylene-3,4-dicarboximide on NiO electrodes. *Chem. Sci.* **2017**, *8*, 541–549. [CrossRef]
30. El-Shaarawy, M.; El-rafa, M.A.; Gouda, M.; Khoder, H.; Ramadan, M. Electrical and Optical Properties for Nano $(SiO_2)_{100-x}$:$(NiO)_x$ Glass Matrix. *IOSR J. Appl. Phys.* **2014**, *6*, 18–29. [CrossRef]
31. Díaz, C.; Valenzuela, M.L. Metallic Nanostructures Using Oligo and Polyphosphazenes as Template or Stabilizer in Solid State. In *Encyclopedia of Nanoscience and Nanotechnology*; Nalwa, H.S., Ed.; American Scientific Publishers: Valencia, CA, USA, 2010; Volume 16, pp. 239–256.
32. Wang, X.; Li, X.; Sun, X.; Li, F.; Wang, Q.; He, D. Nanostructured NiO electrode for high rate Li-ion batteries. *J. Mater. Chem.* **2011**, *21*, 3571–3573. [CrossRef]
33. Dar, F.I.; Moonooswamy, K.R.; Es-Souni, M. Morphology and property control of NiO nanostructures for supercapacitor applications. *Nanoscale Res.* **2013**, *8*, 1–7. [CrossRef]
34. Duan, H.; Zheng, X.; Yuan, S.; Li, Y.; Tian, Z.; Deng, Z.; Su, B. Sub-3 nm NiO nanoparticles: Controlled synthesis, and photocatalytic activity. *Mater. Lett.* **2012**, *81*, 245–247.
35. Wang, C.; Li, J.; Liang, X.; Zhang, Y.; Guo, G. Photocatalytic organic pollutants degradation in metal–organic frameworks. *Energy Environ. Sci.* **2014**, *7*, 2831–2867. [CrossRef]
36. Ukoba, K.O.; Eloka-Eboca, A.C.; Inambao, F.L. Review of nanostructured NiO thin film deposition using the spray pyrolysis technique. *Renew. Sustain. Energy Rev.* **2018**, *82*, 2900–2915. [CrossRef]
37. Carlucci, C.; Xu, H.; Scremin, B.F.; Giannini, C.; Sibillano, T.; Carlino, E.; Videtta, V.; Gigli, G.; Ciccarella, G. Controllable one-pot synthesis of anatase TiO_2 nanorods with the microwave-solvothermal method. *Sci. Adv. Mater.* **2014**, *6*, 1668–1675. [CrossRef]
38. Allende-González, P.; Laguna-Bercero, M.A.; Barrientos, L.; Valenzuela, M.L.; Díaz, C. Solid State Tuning of TiO_2 Morphology, Crystal Phase, and Size through Metal Macromolecular Complexes and Its Significance in the Photocatalytic Response. *ACS Appl. Energy Mater.* **2018**, *7*, 3159–3170. [CrossRef]
39. Ahmed, M.A. Synthesis and structural features of mesoporous NiO/TiO_2 nanocomposites prepared by sol–gel method for photodegradation of methylene blue dye. *J. Photochem. Photobiol. A Chem.* **2012**, *238*, 63–70. [CrossRef]
40. Faisal, M.; Harraza, F.A.; Ismailc, A.A.; El-Tonib, A.M.; Al-Sayaria, S.A. Novel mesoporous NiO/TiO_2 nanocomposites with enhanced photocatalytic activity under visible light illumination. *Ceram. Int.* **2018**, *44*, 7047–7056. [CrossRef]
41. Sim, L.C.; Ng, K.W.; Ibrahim, S.; Saravanan, P. Preparation of Improved p-n Junction NiO/TiO_2 Nanotubes for Solar-Energy-Driven Light Photocatalysis. *Int. J. Photoenergy* **2013**, *2013*. [CrossRef]
42. Gangwar, J.; Gupta, B.K.; Tripathi, S.K.; Srivastava, A.K. Phase dependent thermal and spectroscopic responses of Al_2O_3 nanostructures with different morphogenesis. *Nanoscale* **2015**, *7*, 13313–13344. [CrossRef]
43. Ravichandran, R.; Wang, A.; Wager, J. Solid state dielectric screening versus band gap trends and implications. *Opt. Mater.* **2016**, *60*, 181–187. [CrossRef]
44. Chadi, D.J.; Cohen, M.L. Correlation between the static dielectric constant and the minimum energy gap. *Phys. Lett. A* **1974**, *49*, 381–382. [CrossRef]

45. Kalyanaraman, S.; Shajinshinu, P.M.; Vijayalakshmi, S. Refractive index, band gap energy, dielectric constant and polarizability calculations of ferroelectric Ethylenediaminium Tetrachlorozincate crystal. *J. Phys. Chem. Solid* **2015**, *86*, 108–113. [CrossRef]
46. Ghazal, M.N.; Deparis, O.; De Coninck, J.; Gaigneaux, E.M. Tailored refractive index of inorganic mesoporous mixed-oxide Bragg stacks with bio-inspired hygrochromic optical properties. *J. Mater. Chem. C* **2013**, *1*, 6202–6209. [CrossRef]
47. Kischkat, J.; Peters, S.; Gruska, B.; Semtsiv, M.; Chashnikova, M.; Klinkmuller, M.; Fedosenko, O.; Machulik, S.; Alesksandrova, A.; Monastyrski, G.; et al. Mid-infrared optical properties of thin films of aluminum oxide, titanium dioxide, silicon dioxide, aluminum nitride, and silicon nitride. *Appl. Opt.* **2012**, *51*, 6789–6798. [CrossRef]
48. Hervé, P.; Vandamme, L.K.J. General relation between refractive index and energy gap in semiconductors. *Infrared Phys. Technol.* **1994**, *35*, 609–615. [CrossRef]
49. Kumar, V.; Singh, J.K. Model for calculating the refractive index of different materials. *Indian J. Pure Appl. Phys.* **2010**, *48*, 571–574.
50. Pesika, N.S.; Stebe, K.J.; Searson, P.C. Relationship between Absorbance Spectra and Particle Size Distributions for Quantum-Sized Nanocrystals. *J. Phys. Chem. B* **2003**, *107*, 10412–10415. [CrossRef]
51. Goh, E.G.; Xu, X.; McCormick, P.G. Effect of particle size on the UV absorbance of zinc oxide nanoparticles. *Scr. Mater.* **2014**, *78–79*, 49–52. [CrossRef]
52. Doak, J.; Gupta, R.K.; Manivannan, K.; Ghosh, K.; Kahol, P.K. Effect of particle size distributions on absorbance spectra of gold nanoparticles. *Physica E* **2010**, *42*, 1605–1609. [CrossRef]
53. Gharibshahi, E.; Saion, E. Influence of Dose on Particle Size and Optical Properties of Colloidal Platinum Nanoparticles. *Int. Mol. Sci.* **2012**, *13*, 14723–14741. [CrossRef] [PubMed]

Publisher's Note: MDPI stays neutral with regard to jurisdictional claims in published maps and institutional affiliations.

© 2020 by the authors. Licensee MDPI, Basel, Switzerland. This article is an open access article distributed under the terms and conditions of the Creative Commons Attribution (CC BY) license (http://creativecommons.org/licenses/by/4.0/).